metals

MDPI

Article

Effect of Dissolved CO_2 on the Interaction of Stress and Corrosion for Pipeline Carbon Steels in Simulated Marine Environments

Shamsuddeen Ashurah Abubakar, Stefano Mori and Joy Sumner *

Centre for Energy Engineering, Energy and Sustainability Theme, School of Water, Energy and Environment, Cranfield University, Bedfordshire MK43 0AL, UK; s.abubakar@cranfield.ac.uk (S.A.A.); stefano.mori@cranfield.ac.uk (S.M.)
* Correspondence: j.sumner@cranfield.ac.uk

Abstract: Offshore pipelines are subjected to stresses (e.g., from fluid flow, mechanical vibration, and earth movement). These stresses, combined with corrosive environments and in the presence of trace gases (O_2, CO_2), can increase the pipeline's corrosion rate and potentially lead to cracking. As such, the impact of trace gases such as CO_2 (linked to enhanced oil recovery and carbon capture and sequestration) on corrosion is key to determining whether pipelines are at increased risk. American Petroleum Institute (API) 5L X70 and X100 were exposed as stressed C-rings (80% or 95% of yield strength). The tests were conducted with either N_2 (control) or CO_2 bubbled through 3.5% NaCl, at either 5 °C or 25 °C. Linear polarization resistance was used to assess corrosion rate, while morphology and variation were determined using optical microscopy (generating metal loss distributions) and scanning electron microscopy. The control experiment (N_2) showed that corrosion rates correlated with temperature and stress. In this low O_2 environment, both alloys showed similar trends. Under CO_2 exposure, all samples showed accelerated corrosion rates; furthermore, the morphologies generated were different for the two alloys: undercutting corrosion with discontinuous microcracks (X70) or deep, wide ellipses (X100). Understanding these changes in corrosion response is key when selecting materials for specific operational environments.

Keywords: stress; trace gases; pipeline carbon steels; linear polarization resistance; cumulative probability; corrosion morphology

check for updates

Citation: Abubakar, S.A.; Mori, S.; Sumner, J. Effect of Dissolved CO_2 on the Interaction of Stress and Corrosion for Pipeline Carbon Steels in Simulated Marine Environments. *Metals* **2023**, *13*, 1165. https://doi.org/10.3390/met13071165

Academic Editor: Leu-Wen Tsay

Received: 28 April 2023
Revised: 14 June 2023
Accepted: 19 June 2023
Published: 22 June 2023

Copyright: © 2023 by the authors. Licensee MDPI, Basel, Switzerland. This article is an open access article distributed under the terms and conditions of the Creative Commons Attribution (CC BY) license (https://creativecommons.org/licenses/by/4.0/).

1. Introduction

For decades, carbon steel pipelines have been installed and operated around the globe to transport oil and gas [1]. They are considered to be a safe, effective, and economical means of transportation [2,3]. Pipelines are used as a means of transportation of CO_2. However, CO_2 has been observed to have a strong impact on the corrosion rates of pipeline steels [4,5]. CO_2 enhances cathodic reaction rates and can also have a direct contribution to hydrogen charging of the steel's surface layer, especially when under pressure, resulting in the loss of ductility at tensile loads and the formation of blisters or cracks [5,6]. The risk of hydrogen embrittlement of these steels, associated with CO_2 transportation, is one of the major concerns related to their usage [4]. Research in the past four decades has shown that the diffusion of hydrogen into steel's crystalline structure and certain other alloys or metals causes hydrogen–material interactions and microstructural changes. This can lead to hydrogen embrittlement (HE) and can subsequently lead to hydrogen environmentally assisted cracking (HEAC) [7]. Hydrogen embrittlement is defined as the loss or reduction in tensile strength and the ductility of a metal or alloy due to the diffusion of hydrogen atoms into the metal or alloy's crystalline structure during a corrosion process [8–10]. Due to this reduction in ductility, pipelines can be prone to stress corrosion cracking, which can lead to premature failure. The mechanism of CO_2 corrosion encountered in an aqueous

solution can be explained in the following way: CO_2 combines with H_2O to form H_2CO_3 (carbonic acid). H_2CO_3 then further dissociates into HCO_3^-, H^+, and CO_3^{2-} [11,12].

The major cathodic reactions are the reduction in H^+, H_2CO_3, and HCO_3^- as expressed below [13–16].

$$2H^+_{(aq)} + 2e^- \rightarrow H_{2(g)} \quad (1)$$

$$2H_2CO_{3(aq)} + 2e^- \rightarrow 2HCO_3^-{}_{(aq)} + H_{2(g)} \quad (2)$$

$$2HCO_3^-{}_{(aq)} + 2e^- \rightarrow 2CO_3^-{}_{(aq)} + H_{2(g)} \quad (3)$$

$$2H_2O_{(l)} + 2e^- \rightarrow 2OH^- + H_{2(g)} \quad (4)$$

The major anodic reactions are the dissolution of Fe (iron) followed by $FeCO_3$ (iron carbonate) formation as shown below [13–16].

$$Fe \rightarrow Fe^{2+} + 2e^- \quad (5)$$

$$Fe^{2+} + CO_3^{2-} \rightarrow FeCO_3 \quad (6)$$

Carbon steels in pipeline applications are subjected to two forms of stress corrosion cracking (SCC): high-pH SCC and near-neutral pH SCC [17,18]. High-pH SCC is characterized by an intergranular mode of cracking and has been observed in concentrated carbonate/bicarbonate solutions with pH values higher than 9 [19–22]. On the other hand, near-neutral SCC (pH = 6–8) is characterized by a trans-granular cracking mode and is associated with a dilute carbonate/bicarbonate medium [19–22]. In this research, samples were exposed to a near-neutral environment (solution with N_2) and a slightly acidic environment (solution with CO_2). Several studies have been conducted in various corrosive environments (NS4 solution, saturated CO_2 medium, carbonate/bicarbonate solutions, mixture of CO_2/O_2, CO_2/H_2S medium, 3.5% NaCl solution, etc.) [5,23–26] to understand the stress corrosion cracking behavior of pipeline carbon steels after failure. However, understanding the corrosion behavior with applied stress before the failure of pipeline steels in marine environments saturated with CO_2 has not yet been reported.

The purpose of this study is to investigate the impact of trace gases on the stress corrosion interactions of API 5L X70 and X100 carbon steels in simulated saltwater environments saturated with either N_2 (control condition) or CO_2. Tests were run at 5 °C or 25 °C. To assess the impact of stress, C-ring samples (unnotched) were stressed at 80% or 95% yield strength and notched samples were stressed to 80% yield strength. V-notches were machined across the top center of the C-ring to create a triaxial stress condition adjacent to the root of the notch. To assess the rate of corrosion, linear polarization resistance measurements were performed to monitor the samples' corrosion rates and potentials. Image metrology via optical microscopy was used to measure the metal loss exceedance of each sample and scanning electron microscopy was used to determine the corrosion morphology on the samples' surfaces.

2. Experimental Procedures

2.1. Exposed Materials

The materials exposed in this work are API 5L X70 and X100 carbon steels. As observed from Scanning electron microscopy (SEM, Tescan, Brno—Kohoutovice, Czech Republic). (Figure 1a,b, respectively), the X70 steel is composed of globular ferrite grains with grain boundary pearlite grains and coarse dispersion of precipitates, while the X100 steel is made up of bainitic ferrite grains with finely dispersed austenite grains. This is consistent with the literature [27–30]. The micrographs were obtained by polishing the ground surfaces using a 1 μm diamond suspension to obtain a mirror surface finish and then etched with a

2% nital solution for 15 to 25 s. The chemical compositions of the carbon steels as received from the manufacturers are presented in Table 1.

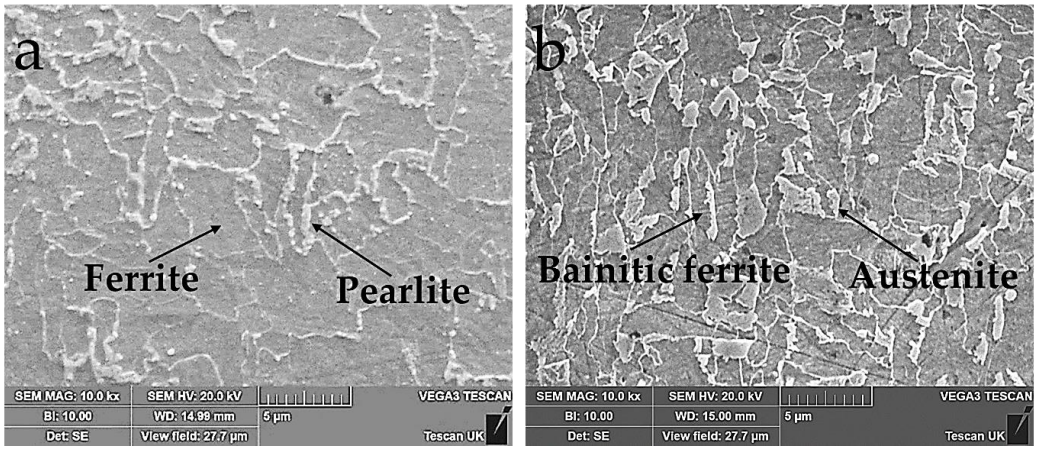

Figure 1. Microstructures of the exposed carbon steels as observed via scanning electron microscopy: (**a**) API 5L X70; (**b**) API 5L X100.

Table 1. Chemical compositions of the API 5L X70 and X100 carbon steels (wt.%).

Grade	C	Si	Mn	P	S	Cr	Mo	Ni	Al	Cu	Nb	Ti	Fe
X70	0.05	0.26	1.66	0.007	0.001	0.02	0.07	0.24	0.045	0.015	0.045	0.015	Bal.
X100	0.06	0.22	1.96	0.007	0.002	0.02	0.18	0.30	0.003	0.210	0.045	0.014	Bal.

2.2. C-Ring Loading Tests

C-ring samples were used to assess the impact of CO_2 in 3.5% NaCl solution on the stress corrosion resistance of API 5L X70 and X100 carbon steels. The samples were designed in accordance with the ASTM G38-01 [31] and NACE TM0177-05 standards [32], using ratios of between 10–100 outer diameter to wall thickness (diameter/thickness) and between 2–10 (width/thickness). This provided final sample dimensions of 18.5 mm outer diameter, 1.3 mm wall thickness, and 12 mm width, finished with a 600 grit (P1200). Figure 2 shows the C-ring design.

A constant strain method was used to stress the specimens to the desired stress levels of 80% and 95% of the yield strength for unnotched samples and notched samples stressed at 80% Y.S. Table 2 shows the as-received yield strength of the carbon steels and calculated desired yield strength. Notched samples were machined by engraving 200 μm V-notches across the top center of the C-ring to create a triaxial stress condition adjacent to the root of the notch on the specimens' surfaces. The stress is exerted on the diameter of the C-ring by tightening a bolt at a calculated distance based on the C-ring's outer diameter, its elastic modulus, and wall thickness as outlined in the ASTM G38-01 standard [31] and shown in Equation (7):

$$OD_f = OD - \Delta; \tag{7}$$

$$\text{where}: \Delta = \frac{f\pi D^2}{4EtZ} \tag{8}$$

$$D = (OD - t) \tag{9}$$

where OD = outer diameter of the C-ring before stressing, mm; OD_f = outer diameter of the stressed C-ring, mm; f = desired stress, MPa; Δ = change in OD giving desired stress, mm; D = mean diameter ($OD - t$), mm; t = wall thickness, mm; E = modulus of elasticity, MPa; and Z = correction factor for curved beams.

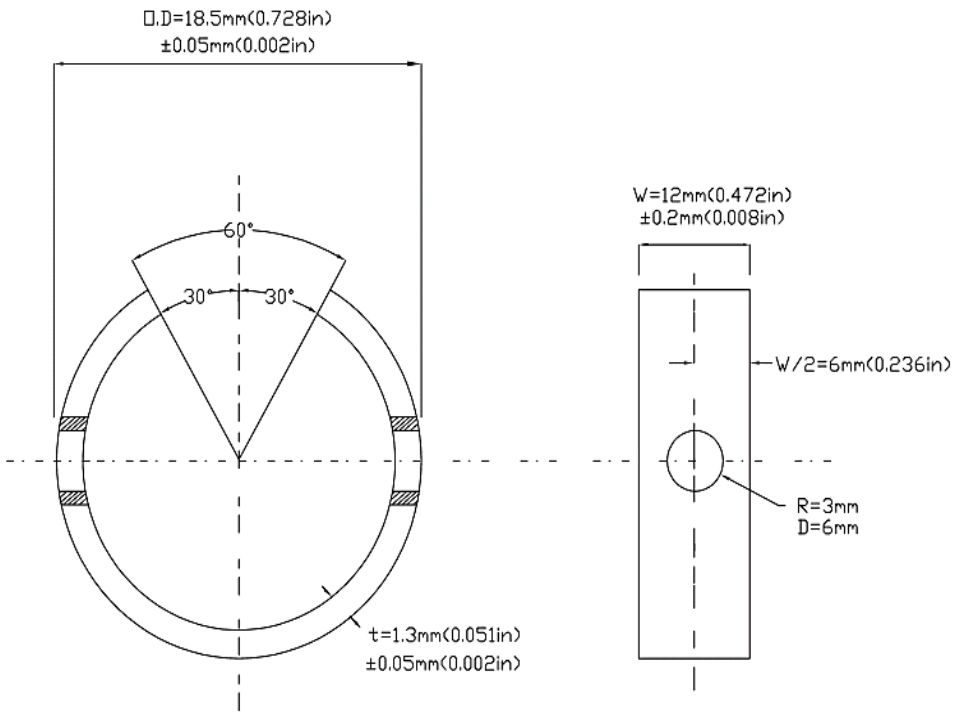

Figure 2. C-ring design and dimensions.

Table 2. The as-received and desired yield strengths of the exposed materials.

Material Grade	Yield Strength, MPa (As Received)	Desired Yield Strength, MPa	
		80% Y.S.	95% Y.S.
X70	510	408.00	484.50
X100	698	558.40	663.10

2.3. Exposure Solutions

Sodium chloride was mixed to give 3.5% salinity (35 g of sodium chloride dissolved in every 1 liter of deionized water). The 3.5% NaCl solution was transferred into a three-electrode electrochemical cell. Figure 3 shows the schematic diagram of the test cell. The test cell solution was then heated or cooled to the desired temperature. The stressed specimens were suspended in the test cell and then the cell was sealed. Depending on the test condition, the desired gas was continuously bubbled in the test cell at 50 mL/min flow rate. N_2 was used to deoxygenate the solution and CO_2 was used to lower the pH from a near-neutral pH of about 7.2 to 5.6 and 6.1 at 5 °C and 25 °C, respectively. The test conditions were maintained for 5 weeks for each experiment. Table 3 presents a summary of the different test conditions and exposed samples.

Table 3. Summary of test conditions.

S/N	Material Grade	Sample Label	Yield Strength, %	Sol. Temp., °C	Gas
1	X70	X70N_2-5a	80	5	N_2
2	X70	X70N_2-5b	95	5	N_2
3	X70	X70N_2-Notched-5	80	5	N_2
4	X70	X70N_2-25a	80	25	N_2
5	X70	X70N_2-25b	95	25	N_2

Table 3. *Cont.*

S/N	Material Grade	Sample Label	Yield Strength, %	Sol. Temp., °C	Gas
6	X70	X70N_2-Notched-25	80	25	N_2
7	X70	X70CO_2-5a	80	5	CO_2
8	X70	X70CO_2-5b	95	5	CO_2
9	X70	X70CO_2-Notched-5	80	5	CO_2
10	X70	X70CO_2-25a	80	25	CO_2
11	X70	X70CO_2-25b	95	25	CO_2
12	X70	X70CO_2-Notched-25	80	25	CO_2
13	X100	X100N_2-5a	80	5	N_2
14	X100	X100N_2-5b	95	5	N_2
15	X100	X100N_2-Notched-5	80	5	N_2
16	X100	X100N_2-25a	80	25	N_2
17	X100	X100N_2-25b	95	25	N_2
18	X100	X100N_2-Notched-25	80	25	N_2
19	X100	X100CO_2-5a	80	5	CO_2
20	X100	X100CO_2-5b	95	5	CO_2
21	X100	X100CO_2-Notched-5	80	5	CO_2
22	X100	X100CO_2-25a	80	25	CO_2
23	X100	X100CO_2-25b	95	25	CO_2
24	X100	X100CO_2-Notched-25	80	25	CO_2

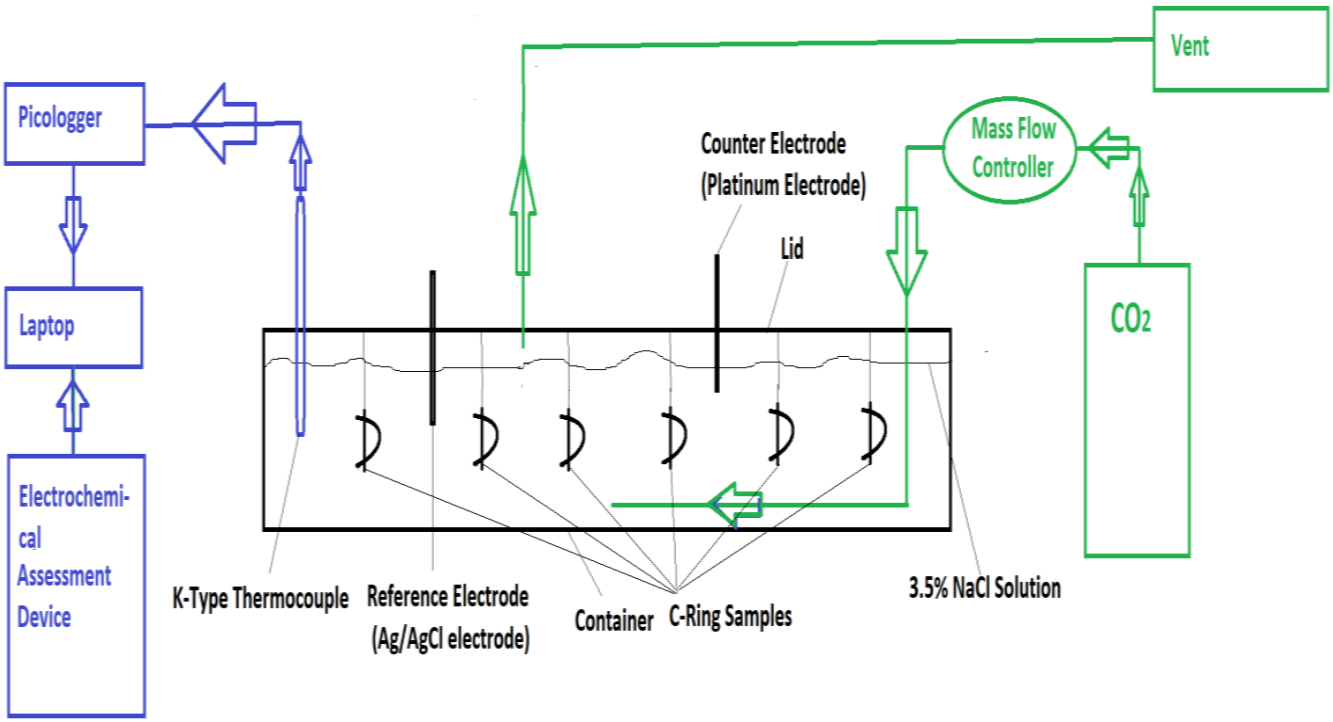

Figure 3. Schematic diagram of the test cell.

2.4. Electrochemical Analysis: Linear Polarization Resistance Measurements

Linear polarization resistance measurements were taken to monitor the samples' corrosion rates and potentials. The working electrode (specimen) was polarized at a potential of ±10 mV around its corrosion potential with a slow scan rate of 0.167 mV/s to maintain conditions close to a steady state as reported by Papavinasam and Baboian [8,33]. Periodic polarizations of the whole area of C-rings directly exposed to the solutions were carried out to monitor the change in corrosion rates and potentials after every 168 h of exposure.

The corrosion rate of a specimen after polarization was calculated using the Stern–Geary Equation (10) [33–35]:

$$I_{corr} = \frac{B}{R_P}; \tag{10}$$

$$\text{where}: \ B = \frac{\beta_a \cdot \beta_c}{2.303(\beta_a + \beta_c)} \tag{11}$$

in which I_{corr} = total anodic current, µA; B = Stern–Geary constant with a value of 25 for carbon steels exposed to seawater conditions as outlined in NACE corrosion engineer's reference book [33] and Papavinasam [8], V; R_p = linear polarization resistance of the electrode, $\Omega.cm^2$; β_a = slope of the anodic Tafel reaction, V/decade; and β_c = slope of the cathodic Tafel reaction, V/decade.

Based on Faraday's law, the corrosion rate (CR) can be calculated using Equation (12) [33–35]:

$$CR(\frac{mm}{y}) = K_{corr}\left(\frac{i_{corr}}{\rho_{metal}}\right)EW \tag{12}$$

$$\text{where}: i_{corr} = \frac{I_{corr}}{A} \tag{13}$$

$$EW = \frac{A_{wt}}{n} \tag{14}$$

in which K_{corr} = corrosion constant with a value of 3.27×10^{-3}, mm g/µA (cm yr); ρ = density of alloy, g/cm^3; i_{corr} = corrosion current density, µA/cm^2; I_{corr} = total anodic current, µA; A = exposed sample area, cm^2; EW = equivalent weight; A_{wt} = atomic weight of the element, Dalton (Da); and n = valence of the element.

Corrosion rate errors were calculated using the propagation of error method as outlined by Taylor [36]. The calculated error was observed to be very negligible in the magnitude of 10^{-5} to 10^{-7} mm/yr.

2.5. Post-Exposure Analysis

Scanning electron microscopy (SEM, Tescan, Brno—Kohoutovice, Czech Republic), energy dispersive spectroscopy (EDS, Oxford Instruments Inc., Oxfordshire, United Kingdom), and X-ray diffraction (XRD, Siemens, Munich, Germany) analysis were carried out on the exposed samples. The scanning electron microscopy images and energy dispersive spectroscopy (EDS) data were obtained via a Tescan Vega 3 Large SEM and Oxford Instruments AztecEnergy V2.2 with AztecHKL V2.2 software (Oxford Instruments Inc., Oxfordshire, United Kingdom). An error of ±5% was assumed for all EDS measurements [37]. The X-ray diffraction analysis was carried out using a Siemens D5005 X-Ray Diffractometer and a Bruker DIFFRAC plus XRD Commander V2.4.1 with EVA V5.0 software (Siemens, Munich, Germany). Dimensional metrology was also conducted on the stress-oriented sections of the exposed samples in accordance with Sumner et. al. [38,39]. Figure 4 show the stages of the dimensional metrology technique to determine the metal loss.

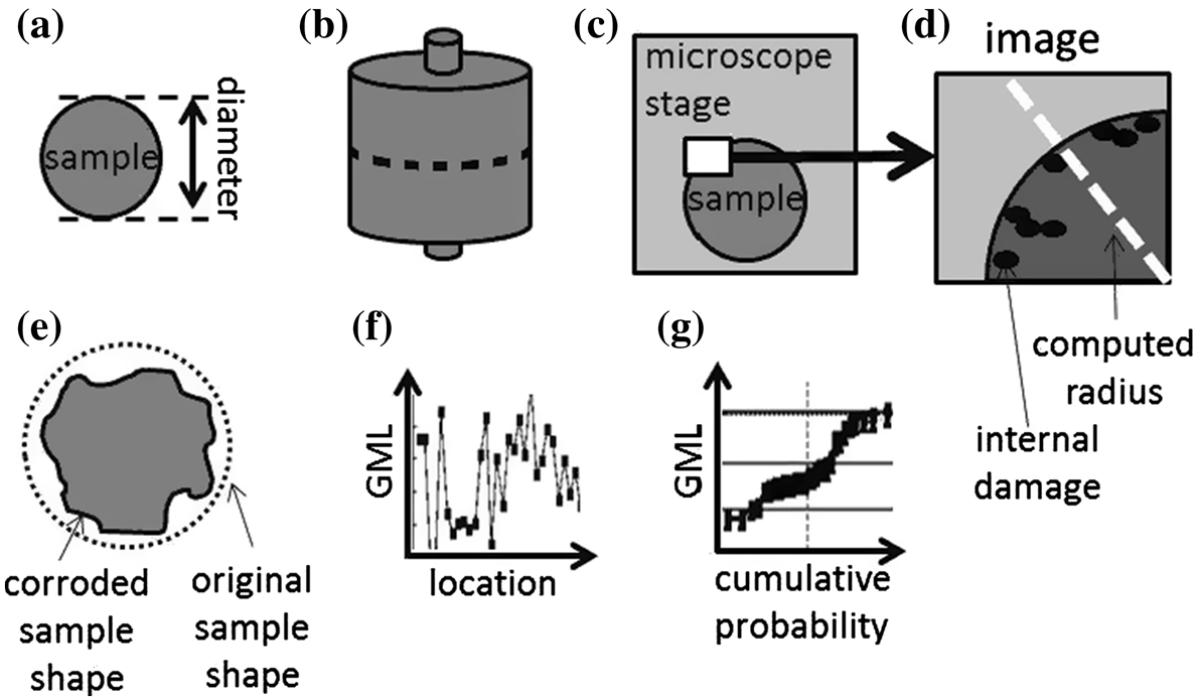

Figure 4. Dimensional metrology technique stages to determine metal loss of the exposed samples. Reprinted with permission from Refs. [38,39]. 2015 Taylor & Francis. (**a**) Pre-exposure dimensions are taken from the samples; (**b**) the samples are then exposed and cross-sectioned at a high-stress point; (**c**) the samples are placed on an x–y calibrated Leitz Wetzlar AxioCam ICc 1 microscope (Zeiss group, Oberkochen, Germany) stage with an image analyzer subroutine to measure evenly spaced images of the sample; (**d**) key points such as internal damage and remaining metal on the image are selected; (**e**) comparison of pre- and post-exposure sample radii; (**f**) acquiring a range of different metal losses or internal damage, formed oxides, or scale thicknesses around the sample; and (**g**) data ordering from most to least damaged to give the cumulative probability of damage [38,39]. The collected data are plotted against cumulative normal distribution (in standard deviations) with a metal loss error of ±5 μm.

3. Results and Discussion

3.1. Corrosion Rates and Potentials

Figure 5a–d present the corrosion rates and potentials of the exposed X70 carbon steel samples in solution with N_2 at 5 °C and 25 °C.

As shown in Figure 5c, continuous increases in corrosion rates with time were observed with a maximum value of 0.0307 mm/year for the sample stressed to 95% Y.S. at 788 h at 25 °C; however, a decrease was observed for the sample stressed to 80% Y.S. and the notched sample at 620 h of exposure. Corrosion rate fluctuations were observed for all samples at 5 °C (Figure 5a). A decrease in corrosion rates was observed for samples stressed at 80% Y.S. and 95% Y.S. at 644 h of exposure; however, a decrease was observed for the notched sample at 477 h of exposure. This trend in corrosion rates could be explained to occur as a result of the continuous formation and rupture of their formed surface films (iron oxide). This causes fluctuations in the cathodic reaction rates taking place on the samples' surfaces, leading to variations in corrosion rates with time. The samples stressed at 80% Y.S. and 95% Y.S. (Figure 5a,c, respectively) were observed to show higher corrosion rates. This occurred as a result of an error in the placement of the samples in the test cell, which led to differential aeration on the exposed samples. Different corrosion potentials were observed on the exposed carbon steels in the simulated 3.5% NaCl solution. This shows the change in the thermodynamic behavior of the different steels with a change in the material's microstructure and solution temperature. A continuous increase in potential was observed throughout the duration of the experiment (Figure 5d) with a maximum value

of −718 $mV_{Ag/AgCl}$ obtained from the sample stressed to 95% of Y.S. at 25 °C. At 5 °C, a decrease in potential was observed for all samples at 648 h of exposure, with a maximum value of −754 $mV_{Ag/AgCl}$ observed for the sample stressed at 80% Y.S. (Figure 5b).

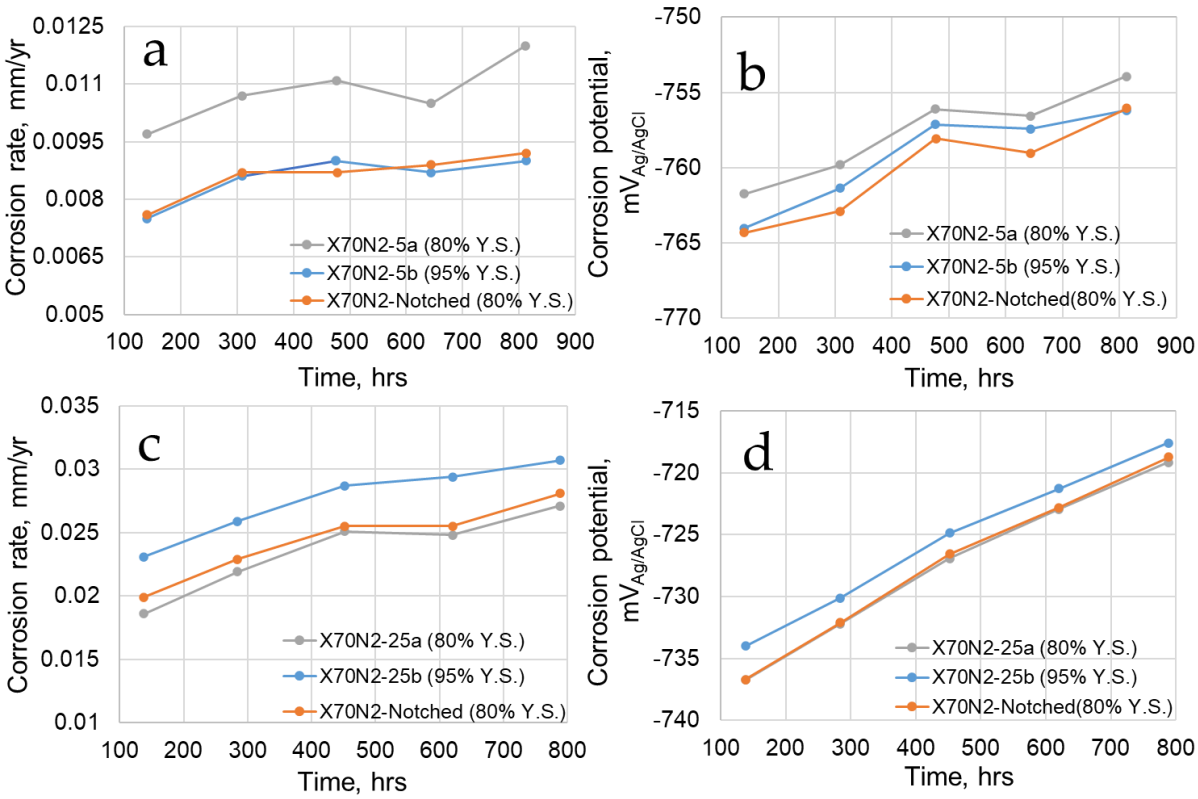

Figure 5. Corrosion rates and potentials of the exposed X70 carbon steel C-rings in simulated saltwater solution with N_2: (**a**) corrosion rates at 5 °C; (**b**) potentials at 5 °C; (**c**) corrosion rates at 25 °C; and (**d**) potentials at 25 °C.

It is observed that the obtained experimental corrosion rate values were lower than the corrosion rates of carbon steels in seawater with a value of 0.13–0.41 mm/year reported by Davies and Michael [40,41], 0.102–0.178 mm/year by Fontana [42], and a value of 0.1 mm/year in quiet seawater to a maximum of 0.75 mm/year at 3 m/s seawater velocity reported by Kreysa and Schutze [43]. These results are due to the continuous bubbling of nitrogen gas in the test solution, which eliminates any entrained air or oxygen with the consequence of lowering the corrosion rate.

The X100 samples (Figure 6a,c) were observed to have higher corrosion rates with a maximum of 0.0362 mm/year for the notched sample in comparison with the X70 samples in solution with N_2 at 25 °C. This shows that the presence of N_2 gas in the solutions has not much of an effect on the corrosion rate of the different exposed carbon steels. Similarly, fluctuations in corrosion rates and potentials with time were observed on the X100 samples at both 5 °C and 25 °C. A decrease in corrosion rate was observed for the sample stressed at 80% Y.S. and the notched sample at 648 h of exposure at 5 °C. However, a continuous decrease was observed for the sample stressed to 95% Y.S. after 648 h. Similarly, lower corrosion rates were observed on the notched sample relative to the un-notched samples, as in the case of X70 samples stressed at 80% Y.S. and 95% Y.S. (Figures 5a and 5c, respectively). This can also be explained to occur as a result of differential aeration in the test cell. A continuous increase in corrosion rates with time was observed on all samples at 25 °C. Maximum potential values of −742 $mV_{Ag/AgCl}$ and −705 $mV_{Ag/AgCl}$ (Figure 6b,d), respectively, were observed for the samples stressed at 80% Y.S. at 5 °C and 25 °C. In general, corrosion potential values were observed to change with solution temperature and

material grade. More negative potential values were observed on all samples exposed at 5 °C.

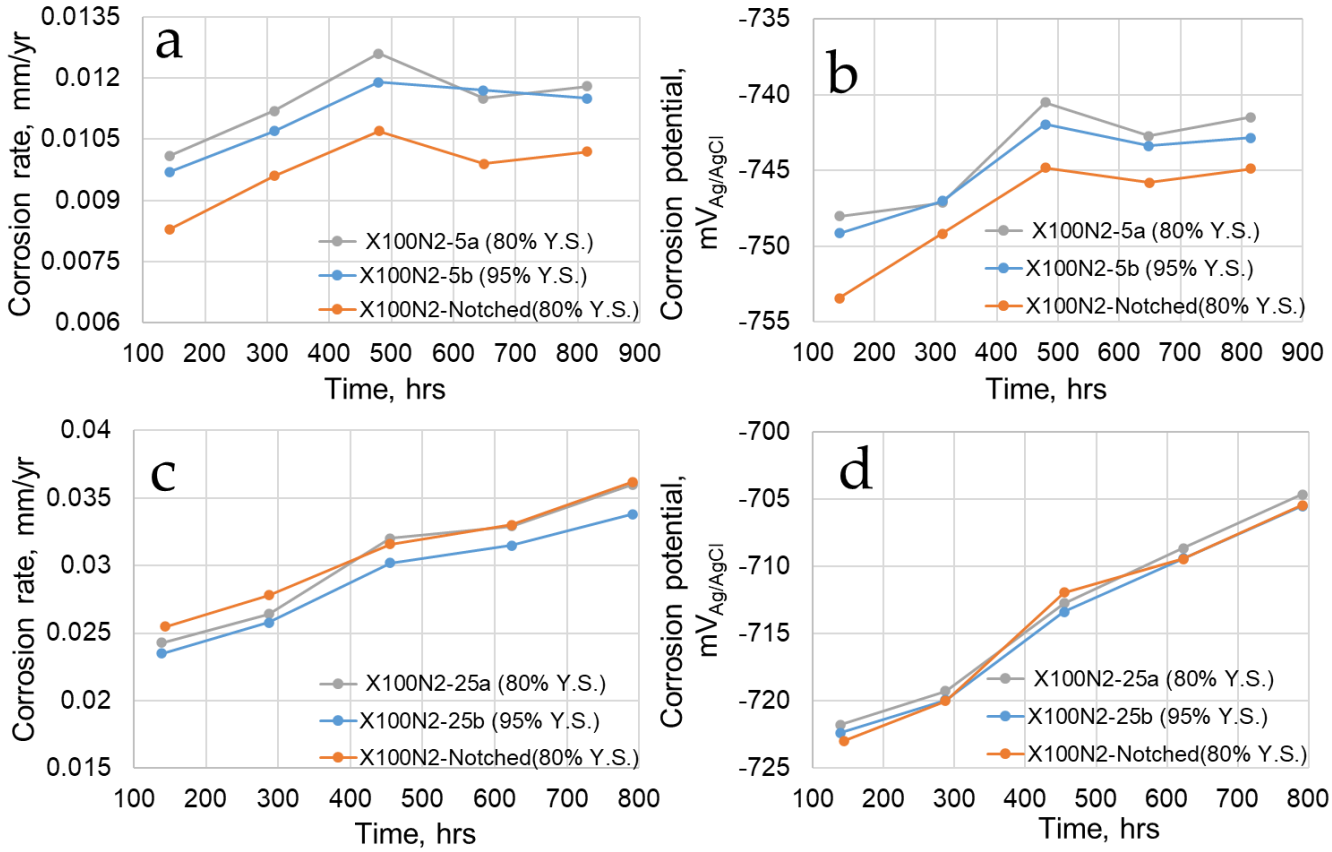

Figure 6. Corrosion rates and potentials of the exposed X100 carbon steel C-rings in simulated saltwater solution with N_2: (**a**) corrosion rates at 5 °C; (**b**) potentials at 5 °C; (**c**) corrosion rates at 25 °C; and (**d**) potentials at 25 °C.

The corrosion rates obtained from the X70 samples exposed to solution with CO_2 (Figure 7a,c) were observed to be much higher than those obtained from solution with N_2. Figure 7a–d present the corrosion rates and potentials of the X70 samples exposed to CO_2 medium at 5 °C and 25 °C. It was observed that the higher the applied stress level, the higher the corrosion rates, while at 25 °C, the higher the applied stress, the lower the corrosion rates. A maximum corrosion rate value of 1.405 mm/year and a minimum of 0.8521 mm/year was obtained for the sample stressed to 80% Y.S. at 25 °C. The calculated corrosion rate values are more or less similar to the values reported by Zhang et al. [44]. A value of 0.9911 mm/year was observed on X70 carbon steel exposed to a soil-extracted solution saturated with 100% CO_2 at ambient temperature. Similarly, Silva et al. [4] reported a corrosion rate value of 1 mm/year to 1.3 mm/year observed on X65 carbon steel exposed to 3.5% NaCl solution saturated with CO_2. Several literature-based predictive models have been developed to forecast corrosion rates of pipelines in CO_2-containing solutions, namely, empirical/semi-empirical, elementary mechanistic, and comprehensive mechanistic models [45]; other predictive models include principal component analysis (PCA), multi-layer perceptron neural network (MLPNN), multiple linear regression (MLR), and radial basis function neural network (RBFNN) models [46]. Alsalem et al. [47] developed a model to estimate the corrosion rate of carbon steel in CO_2-saturated NaCl solution at 25 °C. The predictive model forecast corrosion rate value (about 1.21 mm/year) was similar to our observed corrosion rate, with a maximum value of 1.405 mm/year and a minimum of 0.8521 mm/year. However, the model did not take into consideration the impact of stress on the corrosion of the tested specimens.

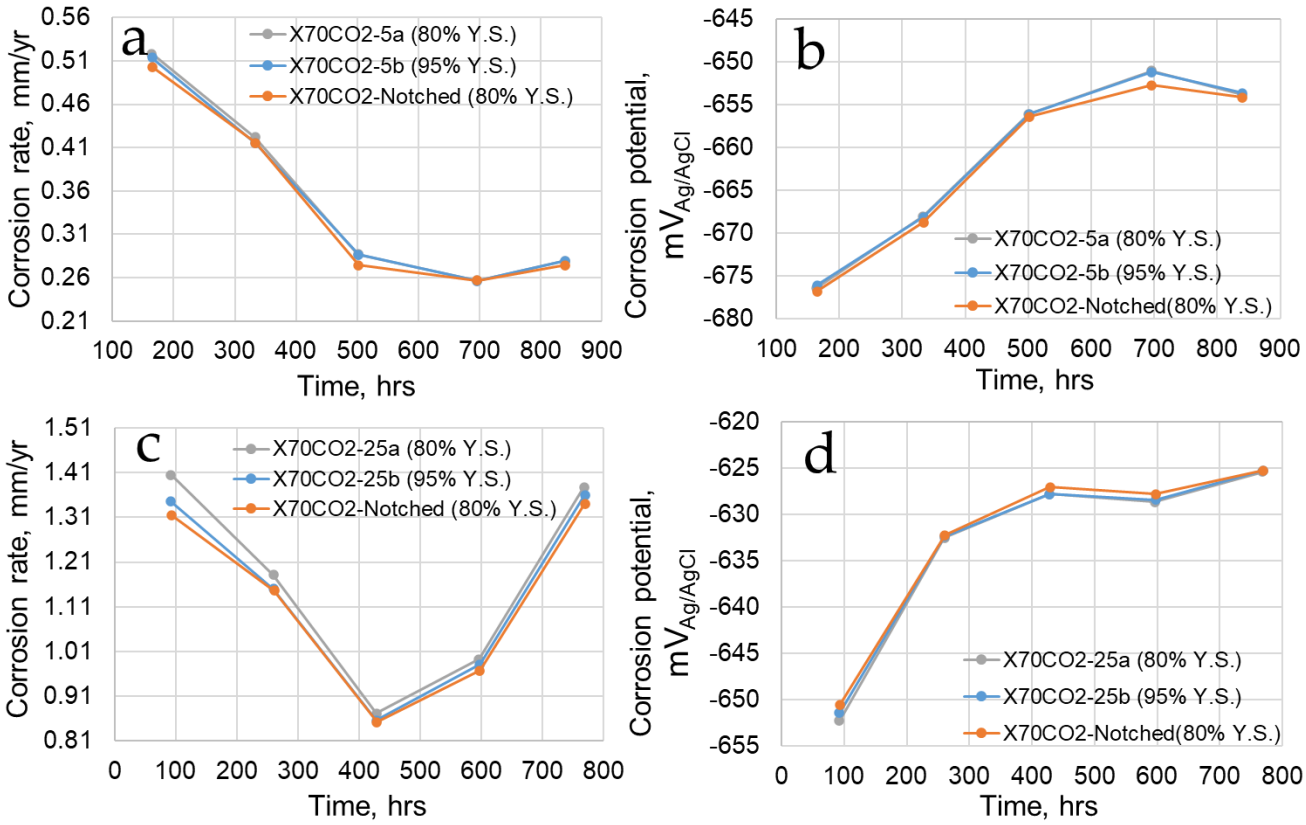

Figure 7. Corrosion rates and potentials of the exposed X70 carbon steel C-rings in simulated saltwater solution with CO_2: (**a**) corrosion rates at 5 °C; (**b**) potentials at 5 °C; (**c**) corrosion rates at 25 °C; and (**d**) potentials at 25 °C.

The corrosion rates of the X100 samples (Figure 8a,c) were observed to decrease with increasing applied stress levels at 5 °C, while at 25 °C the corrosion rate increased with increasing applied stress. This trend in corrosion rate variations could be said to occur as a result of stressed-induced diffusion of the formed oxides into the steel's microstructure [48,49]. This phenomenon depends on changes in the solution temperature and the carbon steel's microstructure. Figure 8a,d show the corrosion rates and potentials of the exposed X100 carbon steels. Maximum and minimum corrosion rate values of 2.8211 mm/year and 1.7141 mm/year at 264 h and 770 h of exposure were observed on the notched sample at 25 °C. Gadala and Alfantazi [50] reported a corrosion rate value of 2.3360 mm/year observed on X100 carbon steel exposed to NS4 soil solution saturated with CO_2 at 25 °C. In general, the corrosion rates of X70 at 5 °C were observed to continuously decrease with time, with a continuous increase for the X100 samples. At 25 °C, a continuous increase was observed after 429 h of exposure time for the X70 samples, with a decrease after 264 h of exposure for the X100 samples. In general, the X100 samples at all exposure conditions were observed to show higher corrosion rates relative to the X70 samples. This indicates that the X100 samples have higher corrosion current density, which leads to higher corrosion rates. Variations in corrosion potentials were observed on all exposed material grades with changes in solution temperature. At 5 °C, a decrease in potential was only observed for the X70 samples at 840 h, with a continuous increase for the X100. A decrease in potential was observed at 597 h and 432 h of exposure, respectively, for the X70 and X100 samples at 25 °C. A maximum potential of −625 $mV_{Ag/AgCl}$ was obtained for the X70 notched sample stressed to 80% Y.S., and −604 $mV_{Ag/AgCl}$ for the X100 notched sample at 25 °C. This clearly indicates variation in the thermodynamic behavior of the different material grades with changes in microstructures and solution temperatures. As observed in Figure 7b,d and Figure 8d, variations in the corrosion rates and the trend in the potentials can occur on samples, as the potential only serves as an indication of the thermodynamic

behavior of the steels exposed to a particular environmental condition. The change in thermodynamic behavior can occur as a result of several factors, such as agitation of the solution, differential aeration, temperature changes, thickness, formation or rupture of surface films, etc.

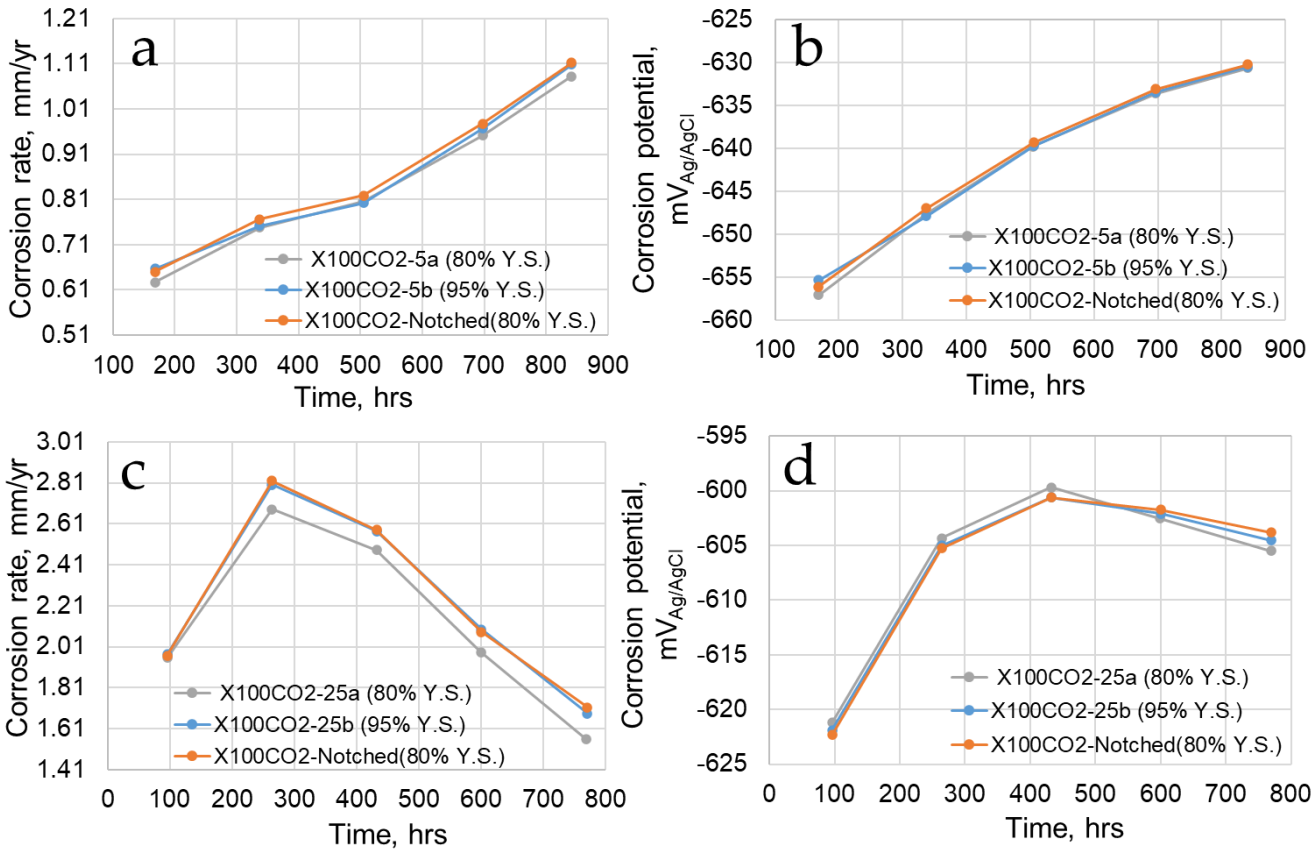

Figure 8. Corrosion rates and potentials of the exposed X100 carbon steel C-rings in simulated saltwater solution with CO_2: (**a**) corrosion rates at 5 °C; (**b**) potentials at 5 °C; (**c**) corrosion rates at 25 °C; and (**d**) potentials at 25 °C.

Variations in corrosion rate trends were observed on the X70 (Figure 7c) and X100 (Figure 8c) samples exposed to solution with CO_2 at 25 °C. The observed change in the corrosion rates occurred with time, with a continuous increase observed in Figure 7c and a continuous decrease in Figure 8c. X-ray diffraction (XRD) analysis was conducted on the exposed samples and revealed the presence of an iron carbonate layer ($FeCO_3$). Figure 9 shows the XRD analysis of an X70 sample exposed at 25 °C. This implies that the steels were able to form a surface layer of iron carbonate in the saturated CO_2 solution, which could serve as a protective film on the surfaces, thereby decreasing the corrosion rate [4,47,50]. Its effect decreases the cathodic reaction rate by surface blocking with the formation of $FeCO_3$ crystals. This hinders the ability of electro-chemically active species to take part in the charge-transfer process [4,51]. The formation of the iron carbonate layer was observed to strongly depend on the microstructure of the steel and the solution's temperature [52]. The obtained corrosion rate values of the exposed samples indicated lower values in comparison with the reviewed literature corrosion rates of carbon steels in CO_2 environments [4]. This can be explained as a result of the low flow rate pressure (atmospheric pressure) that was applied to the CO_2 in the solution [53].

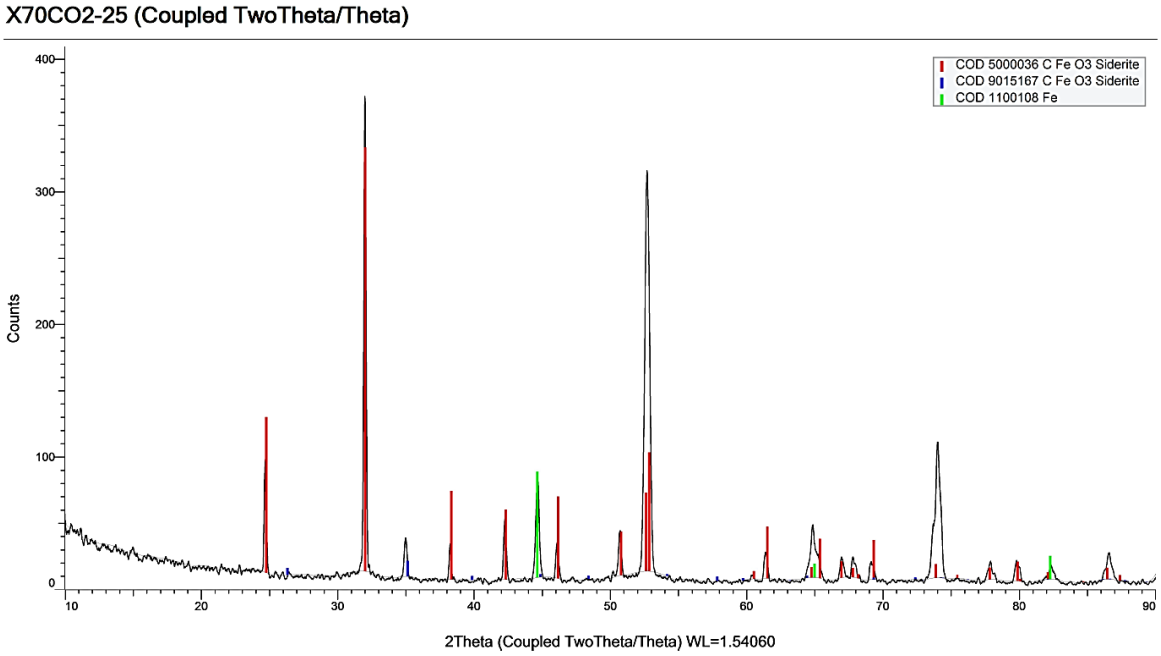

Figure 9. XRD analysis of exposed X70 specimen in simulated saltwater solution with CO_2 at 25 °C after 840 h.

3.2. Cumulative Probability of Metal Loss Exceedance

Dimensional metrology of the samples after an exposed period of 840 h was conducted via optical microscopy. The measured samples' coordinates were used to calculate the cumulative probability of metal loss exceedance. Figure 10a,b, respectively, show the cumulative probability of metal loss exceedance obtained from the datasets of the exposed X70 and X100 samples in solution with N_2 at 25 °C. The dataset for the X70 sample stressed at 80% Y.S. shows a relatively low metal change over half of the sample surface. An even distribution of metal loss was observed over most of the sample that was stressed at 95% Y.S., with the significant formation of pits below the 6% or less probability level. The notched sample presented a more significant metal change over the sample's surface. The dataset for the X100 samples at all levels of applied stress presents a relatively low metal change throughout the majority of the samples with an even damage distribution.

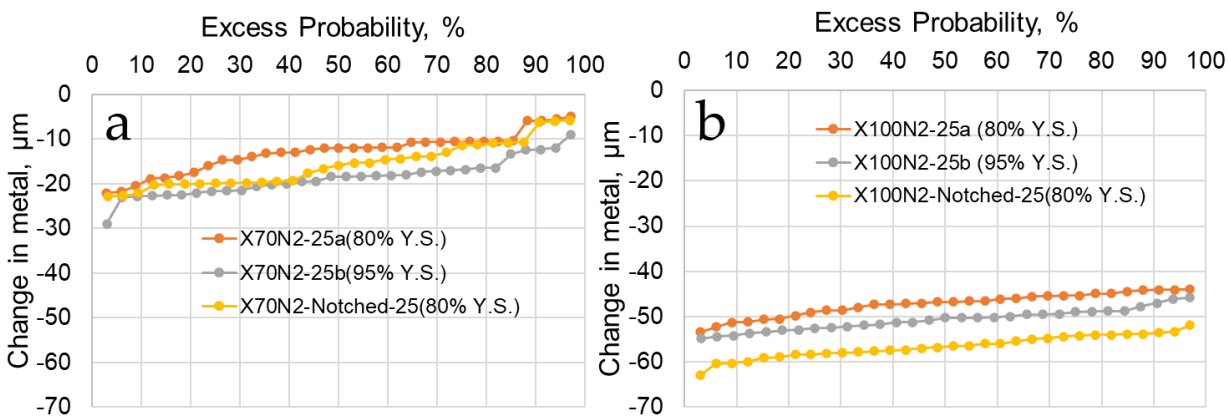

Figure 10. Cumulative probability of metal loss exceedance graphs of C-ring samples exposed to simulated saltwater solution with N_2 at 25 °C: (**a**) X70 samples; (**b**) X100 samples.

Datasets for the X70 and X100 samples exposed to solution with CO_2 at 25 °C as shown in Figure 11a,b, respectively, show a relatively significant metal loss at all stress levels and probability but with low pit features. Relatively even and lower distributions

of metal change were observed on the X70 sample stressed at 95% Y.S., with higher pit formation below the 12% probability level for the sample stressed to 80% Y.S. The X100 notched sample presented a higher probability of about 24% or less to form pitting on the sample's surface. The calculated corrosion rates of the exposed samples tally with the obtained metal loss values when converted to 5 weeks of exposure time. For example, a maximum value of 2.8211 mm/year was calculated for the X100 notched sample; however, converting to a metal loss value of 5 weeks resulted in a value of 271 µm (± 5 µm).

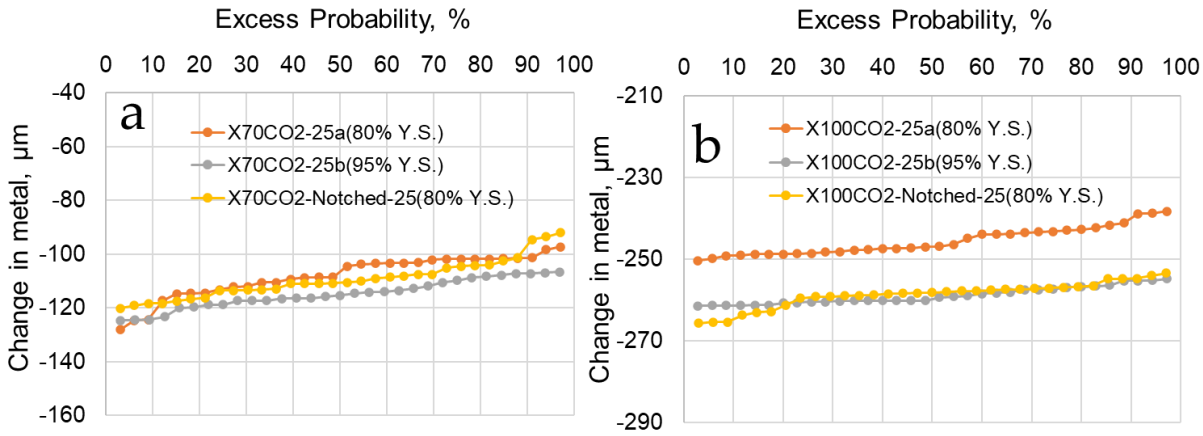

Figure 11. Cumulative probability of metal loss exceedance graphs of C-ring samples exposed to simulated saltwater solution with CO_2 at 25 °C: (**a**) X70 samples; (**b**) X100 samples.

3.3. Scanning Electron Microscopy and EDS Analysis

Conducting scanning electron microscopy analysis of the exposed samples after testing provided a better understanding of the materials' SCC behavior in the tested environmental conditions. Cross-sectional areas of the stress-oriented sections of the exposed samples were examined in order to understand the type of corrosion morphology on the samples' surfaces. Figure 12a,b, respectively, show the SEM images of the X70 samples stressed at 80% Y.S. exposed to solution with N_2 at 5 °C and 25 °C. The samples were observed to show little surface roughness at 25 °C, with a different morphology from that formed at 5 °C. A considerable degree of anodic dissolution was observed on the samples at 5 °C, which was greater at 25 °C.

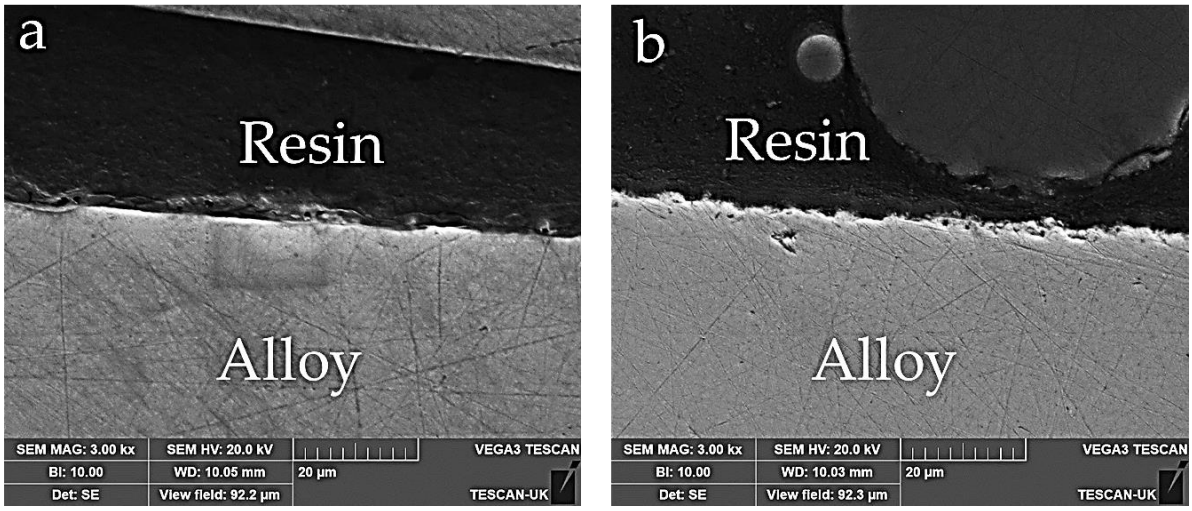

Figure 12. SEM secondary electron images of the exposed X70 C-ring samples in simulated saltwater solution with N_2 stressed at 80% Y.S.: (**a**) at 5 °C; (**b**) at 25 °C.

A clear increase in metal dissolution was observed on the X70 samples exposed to solution with CO_2 at 5 °C and 25 °C stressed at 80% Y.S. as shown in Figure 13a,b, respectively. The corrosion morphologies on the samples exposed at 5 °C were observed to have elliptical but wide and shallow pits, while at 25 °C, the morphologies show a type of deep undercutting metal dissolution. Discontinuous micro-cracks were observed on the samples exposed at 25 °C. This confirms the possibility of SCC occurrence on the carbon steel.

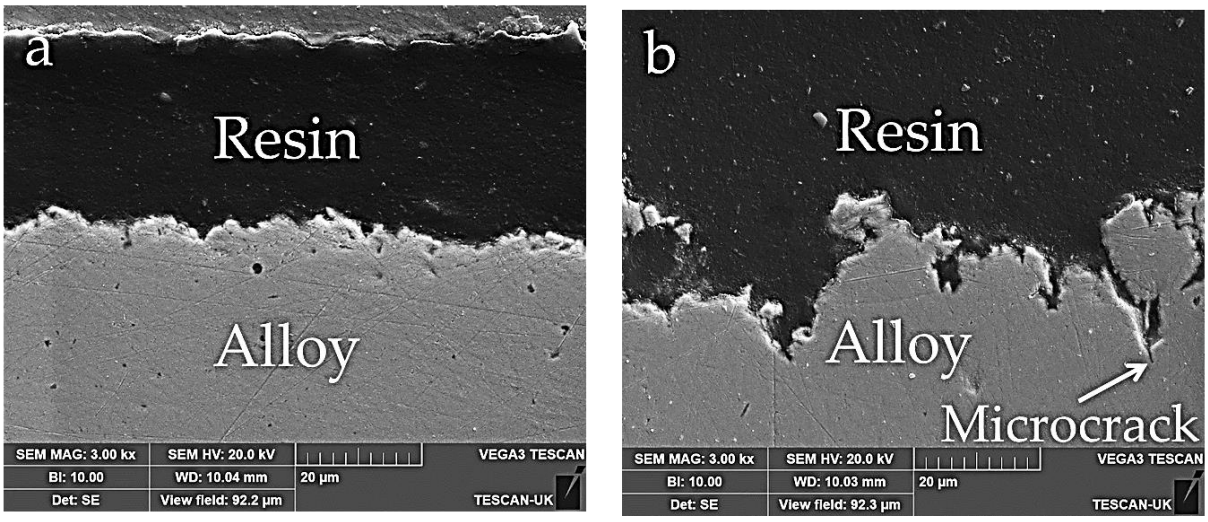

Figure 13. SEM secondary electron images of the exposed X70 C-ring samples in simulated saltwater solution with CO_2 stressed at 80% Y.S.: (**a**) at 5 °C; (**b**) at 25 °C.

The corrosion morphologies of the exposed X100 carbon steels in solution with CO_2 at 5 °C and 25 °C stressed at 80% Y.S., as shown in Figure 14a,b, respectively, presented much wider and deeper elliptical surface corrosion morphologies, which increased with increasing temperature from 5 °C to 25 °C. The variation in corrosion rates and morphologies observed on the exposed carbon steels is said to occur as a result of changes in the microstructure of the carbon steels and the presence of precipitates in their microstructures. The presence of precipitate in a microstructure provides nucleation sites for crack initiation and hydrogen traps, which can lead to hydrogen embrittlement and subsequent stress corrosion cracking [54].

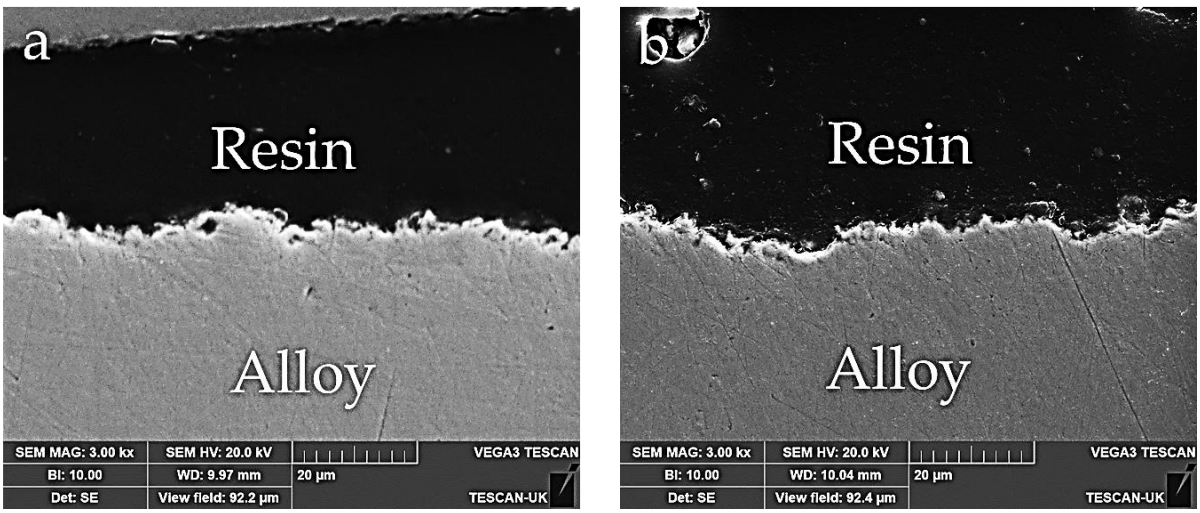

Figure 14. SEM secondary electron images of the exposed X100 C-ring samples in simulated saltwater solution with CO_2 stressed at 80% Y.S.: (**a**) at 5 °C; (**b**) at 25 °C.

In summary, it is observed that CO_2 has a higher impact in comparison with N_2 on the corrosion behavior of the exposed carbon steels. Johnson et al. [55] reported that increasing the amount of CO_2 in near-neutral pH solutions increases the corrosion rates and hydrogen permeation on carbon steels. This is attributed to the ingress of hydrogen atoms into the steel's microstructure, thus reducing its ductility and hence facilitating crack occurrence.

The compositions of the EDS spectra (Figure 15) of the exposed X70 sample in solution with CO_2 at 25 °C stressed at 80% Y.S. are presented in Figure 16 (in weight percentages). Spectrum 1, which is mainly resin, is not reported in the analysis. The carbon content from all spectra is also not reported as EDS does not correctly quantify the percentage of carbon present in the analyzed samples. Approximately equal percentages of Si were observed in spectra 2, 3, and 4 with values of 0.31, 0.29, and 0.33 wt.%, respectively. Increasing percentages of Mn and Fe were observed with the change in spectrum location. Spectrum 4, which is mainly the alloy, presented higher percentages of Mn and Fe (1.89 wt.% and 93.72 wt.%., respectively). In comparison with spectrum 4, a similar value of Fe (93.64 wt.%) was observed in spectrum 3, which is closer to the alloy–resin interface.

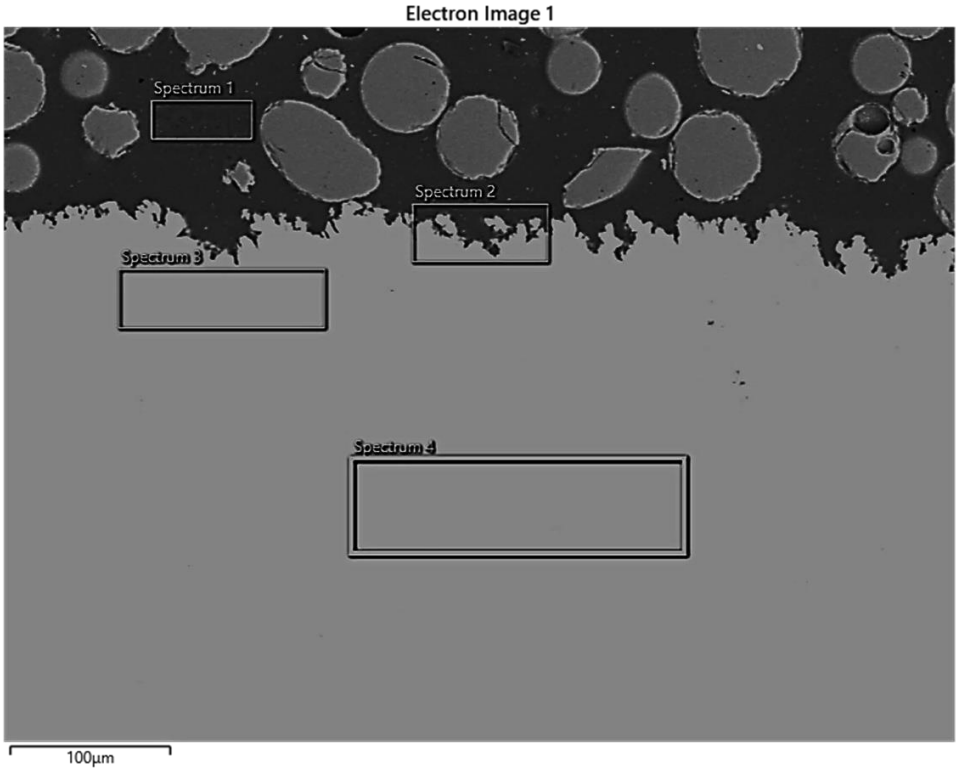

Figure 15. SEM backscattered electron image of exposed X70 carbon steel C-ring in simulated saltwater solution with CO_2 at 25 °C stressed at 80% Y.S. Data from the EDS spectra are reported in Figure 16.

Different compositions of the EDS spectra (Figure 17) of the exposed X100 sample in solution with CO_2 at 25 °C stressed at 80% Y.S. was observed as shown in Figure 18 (in weight percentages). An increased percentage of Si was observed on the analyzed X100 samples, in comparison with the X70 sample. The highest percentage of Si and Mn were observed in spectrum 3 (Figure 18) with a value of 0.98 wt.% and 2.03 wt.%, respectively. Approximately equal percentages of Fe were observed in spectra 3 and 4 (92.2 wt.% and 92.3 wt.%, respectively). Traces of Cl were observed in spectrum 2 with a value of 0.21 wt.%. This can be explained to occur as a result of the simulated 3.5% NaCl solution to which the samples were exposed. In general, no significant differences were observed in the Mn and Fe percentages between the analyzed X70 and X100 samples.

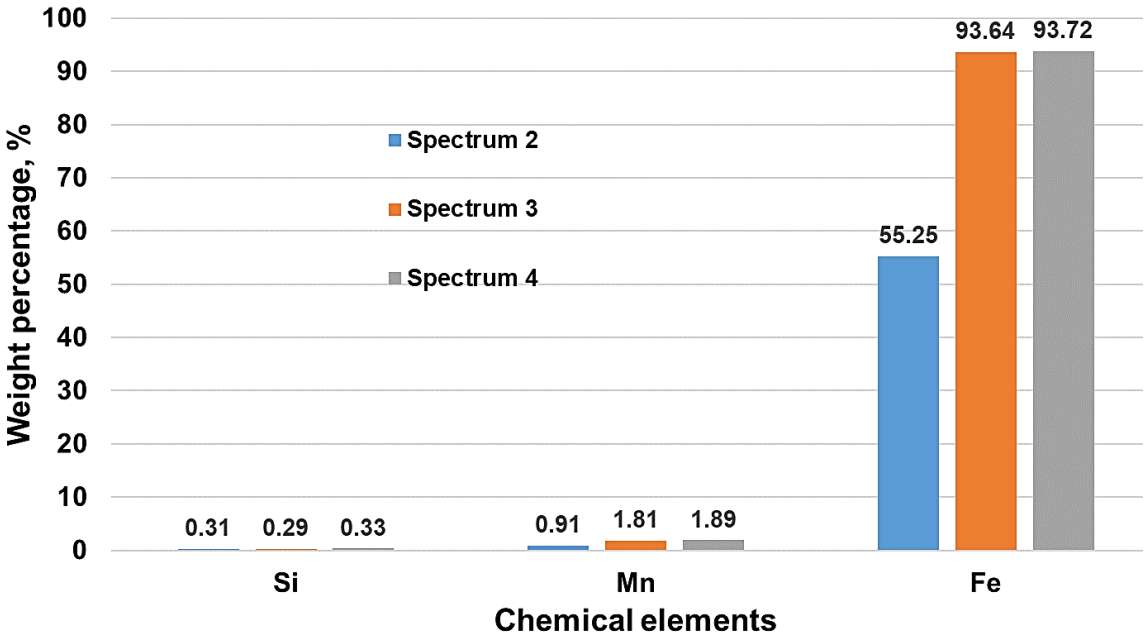

Figure 16. EDS compositions of the exposed X70 sample elements in simulated saltwater solution with CO_2 at 25 °C stressed at 80% Y.S.

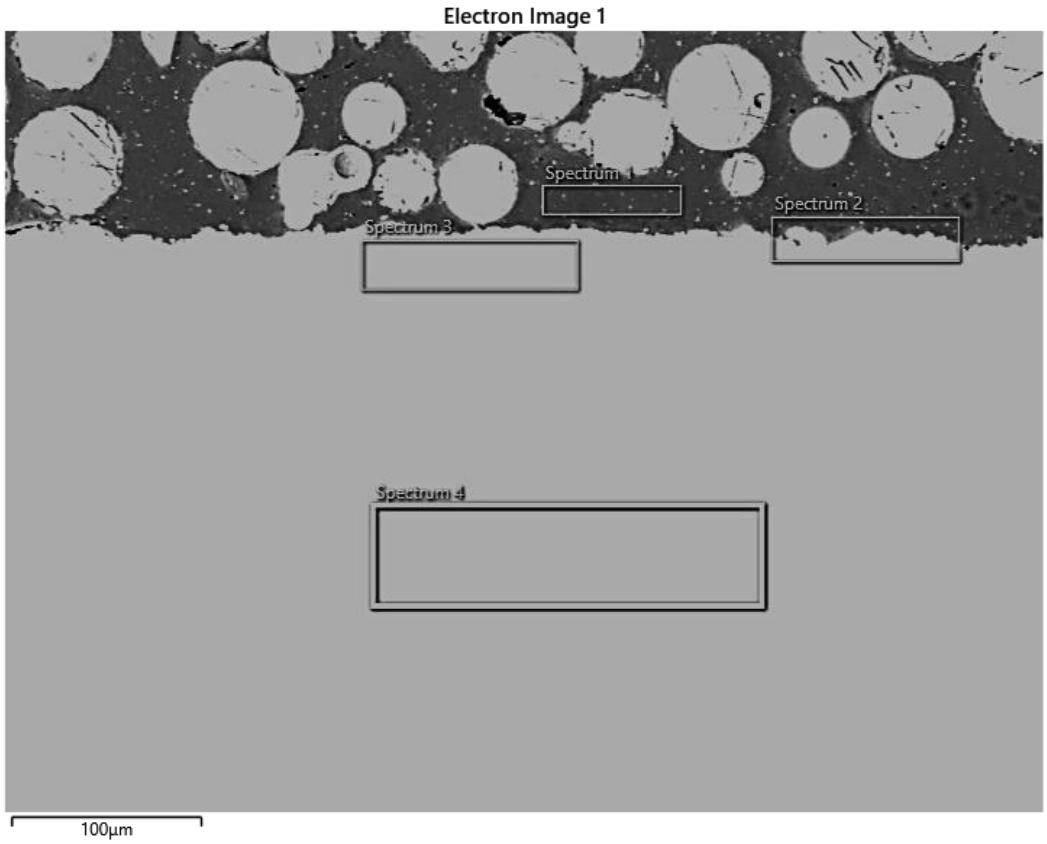

Figure 17. SEM backscattered electron image of the exposed X100 carbon steel C-ring in simulated saltwater solution with CO_2 at 25 °C stressed at 80% Y.S. Data from the EDS spectra are reported in Figure 18.

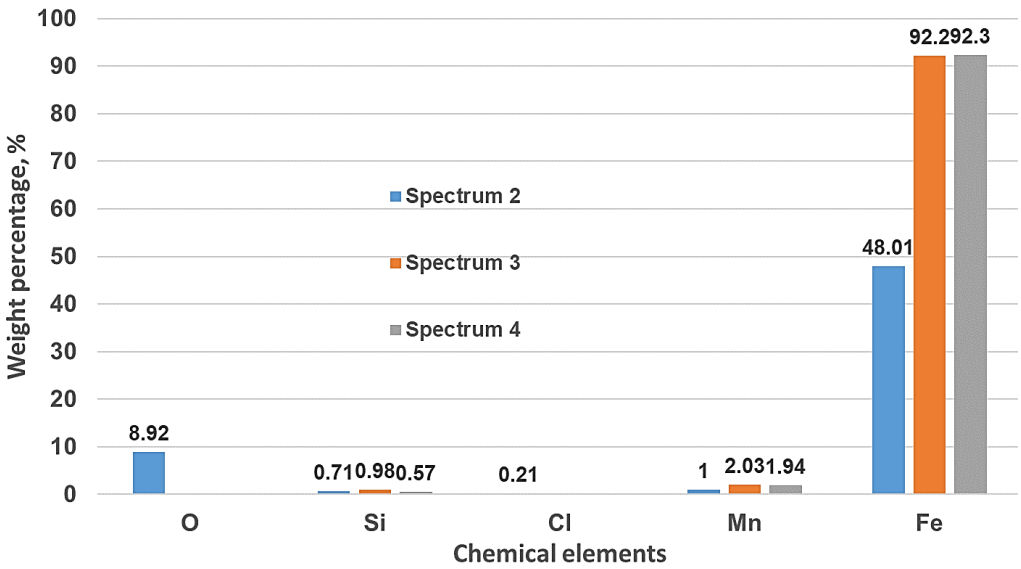

Figure 18. EDS compositions of the exposed X100 sample elements in simulated saltwater solution with CO_2 at 25 °C stressed at 80% Y.S.

In summary, the corrosion rates were observed to increase with time for all X70 samples exposed to solution with N_2, with a maximum value of 0.0307 mm/year for the X70 sample stressed at 95% Y.S. at 25 °C. Variations in the corrosion rate trend were observed for both the X70 and X100 samples exposed to solution with CO_2 at both 5 °C and 25 °C, with a maximum corrosion rate of 1.405 mm/year for the X70 sample stressed at 80% Y.S. and 2.581 mm/year for the X100 notched sample stressed at 80% Y.S. at 25 °C. An increase of more than 100% in corrosion rates was observed on all samples with increasing solution temperatures from 5 °C to 25 °C. The corrosion rate was also observed to increase with increasing the ultimate tensile strength of the exposed carbon steels. It is clearly observed that the X100 samples with bainitic ferrite grains have higher anodic current and obviously higher corrosion current density, which leads to higher corrosion rates. Generally, significant metal change in all samples was observed, with the highest level formation of pits below 12% probability for the X100 notched sample exposed to solution with CO_2. The metal loss was observed to increase with increasing ultimate tensile strength and microstructure of the exposed carbon steels. Different surface roughness was observed on the exposed samples, ranging from even metal dissolution in solution with N_2 to a wide elliptical and undercutting surface morphology in solution with CO_2. The surface roughness of the exposed samples was observed to increase with increasing temperature and change in solution composition from N_2 to CO_2 gas. Discontinuous micro-cracks and higher metal deterioration were observed on the X70 samples exposed to solution with CO_2 at 25 °C stressed at 80% Y.S.

4. Conclusions

Based on the findings of the above-conducted experiments, the following conclusions can be made:

(1) An increase in the solution temperature increased the corrosion rates of the carbon steels. As the temperature increased from 5 °C to 25 °C, the corrosion rate of the exposed carbon steel samples increased by more than 100%.
(2) The corrosion rates of the different exposed alloys (X70 and X100) increased with changes in microstructure and increasing ultimate tensile strength.
(3) The increase in the applied stress levels from 80% Y.S. to 95% Y.S. presented no significant difference in the corrosion rates and metal loss exceedance on the exposed carbon steels in the simulated 3.5% NaCl solution bubbled with either N_2 or CO_2 at both 5 °C and 25 °C.

(4) The formation of an iron carbonate surface layer on the exposed carbon steels in 3.5% NaCl with CO_2 (as detected via XRD) strongly depends on the steel's microstructure and the solution's temperature.
(5) The solution temperature, the microstructure of carbon steels, trace gases, and the applied stress level have direct impacts on corrosion morphology and crack initiation of the exposed carbon steels.

Author Contributions: Conceptualization, S.A.A., S.M. and J.S.; methodology, S.A.A., S.M. and J.S.; software, S.A.A.; validation, S.A.A.; formal analysis, S.A.A.; investigation, S.A.A.; data curation, S.A.A.; writing—original draft preparation, S.A.A.; writing—review and editing, S.M. and J.S.; supervision, S.M. and J.S.; project administration, J.S.; funding acquisition, S.A.A. All authors have read and agreed to the published version of the manuscript.

Funding: We would like to thank the Petroleum Technology Development Fund (PTDF-Nigeria, PTDF/ED/OSS/PHD/SAA/1507/19) and Cranfield University for financial support of this research.

Institutional Review Board Statement: Not applicable.

Data Availability Statement: Data supporting this study are not publicly available due to ethical and legal reasons.

Conflicts of Interest: The authors declare no conflict of interest.

References

1. Liu, H. Introduction. In *Pipeline Engineering*; Lewis Publishers: Boca Raton, FL, USA; CRC Press Company LLC.: Washington, DC, USA, 2003; pp. 1–3.
2. Menon, E.S. Corrosion Protection. In *Pipeline Planning and Construction Field Manual*; Gulf Professional Publishers: Houston, TX, USA; Elsevier: Amsterdam, The Netherlands, 2011; pp. 293–297.
3. Aloqaily, A. Foreword and Book Description. In *Cross Country Pipeline Risk Assessments and Mitigation Strategies*; Gulf Professional Publishing: Houston, TX, USA, 2018; p. 334.
4. Silva, S.C.; Souza, E.A.; Pessu, F.; Hua, Y.; Barker, R.; Neville, A.; Gomes, J.A.D.C.P. Cracking Mechanism in API 5L X65 Steel in a CO_2-Saturated Environment. *Eng. Fail. Anal.* **2019**, *99*, 273–291. [CrossRef]
5. De Oliveira, M.A.; Folena, M.C.; Cruz, S. Comparative Assessment of Environment-Assisted Cracking Susceptibility of Different Grade API 5L Steels in CO_2, CO_2/H_2S, and H_2S Environments. *Steel Res. Int.* **2023**, *2200732*, 1–12. [CrossRef]
6. Shaposhnikov, N.A.; Tsvetkov, N.O.; Strekalovskaya, A.S.; Nikolaeva, D.A.; Devyaterikova, A.G. Physical Modeling of Steel Resistance to Hydrogen Embrittlement. *Key Eng. Mater.* **2023**, *943*, 91–96. [CrossRef]
7. Wei, H.; Djukic, M.B.; Basaran, C. Modeling Fatigue Life and Hydrogen Embrittlement of BCC Steel with Unified Mechanics Theory. *Int. J. Hydrogen Energy* **2023**, *48*, 20773–20803.
8. Papavinasam, S. Monitoring Internal Corrosion. In *Corrosion Control in the Oil and Gas Industry*; Gulf Professional Publishing: Houston, TX, USA; Elsevier: Amsterdam, The Netherlands, 2014; pp. 425–514.
9. Cicek, V. Types of Corrosion. Non-uniform Corr. In *Corrosion Engineering*; John Wiley and Sons: Hoboken, NJ, USA, 2014; pp. 67–70.
10. Sastri, V.S. Introduction and forms of Corrosion. In *Challenges in Corrosion: Costs, Causes, Consequences, and Control*; John Wiley & Sons Inc.: Hoboken, NJ, USA, 2015; pp. 1–95.
11. Cole, I.S.; Corrigan, P.; Sim, S.; Birbilis, N. Corrosion of Pipelines used for CO_2 Transport n CCS: Is it a Real Problem? *Int. J. Greenh. Gas Control* **2011**, *5*, 749–756. [CrossRef]
12. Wei, L.; Pang, X.; Gao, K. Effect of Small Amount of H_2S on the Corrosion Behavior of Carbon Steel in the Dynamic Supercritical CO_2 Environments. *Corros. Sci.* **2016**, *103*, 132–144. [CrossRef]
13. Nesic, S.; Postlethwaite, J.; Olsen, S. An Electrochemical Model for Prediction of Corrosion of Mild Steel in Aqueous Carbon Dioxide Solutions. *Corros. Sci.* **1996**, *52*, 280–294. [CrossRef]
14. Mu, L.J.; Zhao, W.Z. Investigation on Carbon Dioxide Corrosion Behaviour of HP13Cr110 Stainless Steel in Simulated Stratum Water. *Corros. Sci.* **2010**, *52*, 82–89. [CrossRef]
15. Karimi, S.; Taji, I.; Hajilou, T.; Palencsár, S.; Dugstad, A. Role of Cementite Morphology on Corrosion Layer Formation of High-Strength Carbon Steels in Sweet and Sour Environments. *Corros. Sci.* **2023**, *214*, 1–19. [CrossRef]
16. Srivastava, S.; Jacklin, R.; Snellings, R.; Barker, R.; Spooren, J. Experiments and Modelling to Understand $FeCO_3$ Cement Formation Mechanism: Time-evolution of CO_2-species, dissolved-Fe, and pH during CO_2-induced dissolution of Fe (0). *Constr. Build. Mater.* **2022**, *345*, 1–10. [CrossRef]
17. Yang, X.; Sun, F.; Li, Q.; Zhu, R.; Liu, Z.; Du, C.; Li, X. Effect of Hydrogen Charging on the Stress Corrosion Cracking Behavior of X70 Steel in Simulated Deep Seawater Environment. *Metals* **2022**, *12*, 334. [CrossRef]

18. Longfei, S.; Zhiyong, L.; Xiaogang, L.; Xingpeng, G.; Yinxiao, Z.; Wu, W. Influence of Microstructure on Stress Corrosion Cracking of X100 Pipeline sSeel in Carbonate/Bicarbonate solution. *J. Mater. Res. Technol.* **2022**, *17*, 150–165. [CrossRef]
19. Zhang, C.; Ran, M.; Wang, Y.; Zheng, W. Microstructural Effects in the Development of Near-Neutral pH. *Materials* **2022**, *15*, 4372. [CrossRef] [PubMed]
20. Torres-Islas, A.; Gonzalez-Rodriguez, J.G.; Uruchurtu, J.; Serna, S. Stress Corrosion Cracking Study of Microalloyed Pipeline Steels in Dilute $NaHCO_3$ Solutions. *Corros. Sci.* **2008**, *50*, 2831–2839. [CrossRef]
21. Majchrowicz, K.; Brynk, T.; Wieczorek, M.; Miedzi, D. Exploring the Susceptibility of P110 Pipeline Steel to Stress Corrosion Cracking in CO_2-Rich Environments. *Eng. Fail. Anal.* **2019**, *104*, 471–479. [CrossRef]
22. Omura, T.; Amaya, H.; Asahi, H.; Sawamura, M.; Kimura, M.; Ishikawa, N. Near Neutral SCC Properties of Grade X80 Linepipe. In Proceedings of the NACE-International Corrosion Conference and Expo, Atlanta, GA, USA, 22–26 March 2009; pp. 1–16.
23. Alsit, A.; Alkhedher, M.; Hamdan, H. Crack Propagation in Pipelines Under Extreme Conditions of Near-Neutral. *Comput. Mater. Contin.* **2022**, *73*, 5315–5329. [CrossRef]
24. Farhad, F.; Smyth-Boyle, D.; Zhang, X. Fatigue of X65 steel in the Sour Corrosive Environment—A Novel Experimentation and Analysis Method for Predicting Fatigue Crack Initiation Life from Corrosion Pits. *Fatigue Fract. Eng. Mater. Struct.* **2021**, *44*, 1195–1208. [CrossRef]
25. De Motte, R.; Joshi, G.R.; Chehuan, T.; Legent, R.; Kittel, J.; Desamais, N. CO_2 -SCC in Flexible Pipe Carbon Steel Armour Wires. *Corrosion* **2022**, *78*, 547–562. [CrossRef]
26. Jeon, J.; Ahmed, R.; Elgaddafi, R.; Teodoriu, C. Hydrogen Embrittlement of High-Strength API carbon steels in H_2S and CO_2 containing environments. *J. Nat. Gas Sci. Eng.* **2022**, *104*, 1–12. [CrossRef]
27. Bodlos, R. Detailed Microstructure Characterization of a Grade X70 Steel Modified with TiO_2 Using Friction Stir Processing. Master's Thesis, Graz University of Technology, Graz, Austria, 2018; pp. 4–10.
28. Natividad, C.; Falcon, L. Mechanical and Metallurgical Properties of Grade X70 Steel Linepipe Produced by Non-conventional Heat Treatment. In *Characterization of Metals and Alloys*; Springer: Berlin/Heidelberg, Germany, 2017; pp. 3–11.
29. Hwang, B.; Kim, Y.M.; Lee, S.; Kim, N.J.; Ahn, S.S. Correlation of Microstructure and Fracture Properties of API X70 Pipe-line Steels. Research gate. *Metall. Mater. Trans. A* **2005**, *36*, 725–739. [CrossRef]
30. Wang, X.Q.; Yuan, G.; Zhao, J.H.; Wang, G.D. Microstructure and strengthening/toughening mechanisms of heavy gauge pipeline steel processed by ultrafast cooling. *Metals* **2020**, *10*, 1323. [CrossRef]
31. *ASTM G38-01*; Standard Practice for Making and Using C-Ring Stress-Corrosion Test Specimens. ASTM International: West Conshohocken, USA, 2013; Volume 1, pp. 1–8.
32. *NACE TM-0177-05*; Laboratory Testing of Metals for Resistance to Sulfide Stress Corrosion Cracking and Stress Corrosion Cracking in H_2S Environments. NACE International: Houston, TX, USA, 2005.
33. Baboian, R. Corrosion Testing. In *NACE Corrosion Engineer's Reference Book*, 4th ed.; NACE International: Houston, TX, USA, 2016; pp. 115–160.
34. *ASTM G102-89*; Standard Practice for Calculation of Corrosion rates and Related Information from Electrochemical Measurements. ASTM International: West Conshohocken, USA, 2015; Volume 89, pp. 1–7.
35. *ASTM G96-90*; Standard Guide for Online Monitoring of Corrosion in Plant Equipment (Electrical and Electrochemical Methods). ASTM International: West Conshohocken, USA, 2018; Volume 90, pp. 1–10.
36. Taylor, J.R. An Introduction to Error Analysis. In *The Study of Uncertainties in Physical Measurements*, 2nd ed.; Maple-Vail Book Manufacturing Group: Sausalito, CA, USA, 1997; pp. 45–62.
37. Newbury, D.E.; Ritchie, N.W.M. Is scanning electron microscopy/energy dispersive X-ray spectrometry (SEM/EDS) quantitative? *Scanning* **2013**, *35*, 141–168. [CrossRef] [PubMed]
38. Sumner, J.; Simms, N.; Shin, A.; Pearson, J. Kinetics of Duplex Oxide Growth on 9Cr Steels Exposed in CO_2: Application of Dimensional Metrology. *Oxid. Met.* **2017**, *87*, 617–629. [CrossRef]
39. Sumner, J.; Potter, A.; Simms, N.J.; Oakey, J.E. Hot corrosion resistance of gas turbine materials in combusted syngas environments. Mater. *High Temp.* **2015**, *32*, 177–187. [CrossRef]
40. Davies, P.J.B.; Scott, M. Environmental Assisted Cracking. In *Guide to the Use of Materials in Waters*; NACE International: Houston, TX, USA, 2003; pp. 50–53.
41. Davies, P.J.B.; Scott, M. *Oilfield Water Technology*; NACE International: Houston, TX, USA, 2006; pp. 73–77.
42. Fontana, M.G. Stress Corrosion. In *Corrosion Engineering*, 3rd ed.; McGraw-Hill International Book Company: Columbus, OH, USA, 1987; pp. 109–138.
43. Kreysa, G.; Schütze, M. *DECHEMA Corrosion Handbook-Revised and Extended*, 2nd ed.; Dechema: Frankfurt, Germany, 2008.
44. Zhang, L.; Li, X.G.; Du, C.W.; Cheng, Y.F. Corrosion and Stress Corrosion Cracking Behavior of X70 Pipeline Steel in a CO_2-Containing Solution. *ASM Int.* **2009**, *18*, 319–323. [CrossRef]
45. Kahyarian, A.; Singer, M.; Nesic, S. Modeling of uniform CO_2 corrosion of mild steel in gas transportation systems: A review. *J. Nat. Gas Sci. Eng.* **2016**, *29*, 530–549. [CrossRef]
46. Wang, G.; Wang, C.; Shi, L. CO_2 Corrosion Rate Prediction for Submarine Multiphase Flow Pipelines Based on Multi-Layer Perceptron. *Atmosphere* **2022**, *13*, 1833. [CrossRef]
47. Alsalem, M.M.; Ryan, M.P.; Campbell, A.N.; Sedransk, K. Modelling of CO_2 corrosion and $FeCO_3$ formation in NaCl solutions. *Chem. Eng. J.* **2023**, *451*, 1–19. [CrossRef]

48. Phlibeat, J. Diffusion and Stresses. *Defect Diffus. Forum.* **1996**, *129–130*, 3–8.
49. Larché, F.C.; Voorhees, P.W. Diffusion and Stresses: Basic Thermodynamics. *Defect Diffus. Forum.* **1996**, *129–130*, 31–36. [CrossRef]
50. Gadala, I.M.; Alfantazi, A. Electrochemical behavior of API-X100 pipeline steel in NS4, near-neutral, and mildly alkaline pH simulated soil solutions. *Corros. Sci.* **2014**, *82*, 45–57. [CrossRef]
51. Barker, R.; Hua, Y.; Neville, A. Internal corrosion of carbon steel pipelines for dense-phase CO_2 transport in carbon captur and storage (CCS)–A review. *Int. Mater. Rev.* **2017**, *62*, 1–31. [CrossRef]
52. Dugstad, A.; Hemmer, H.; Seiersten, M. Effect of steel microstructure upon corrosion rate and protective iron carbonate film formation. *Corrosion* **2001**, *57*, 369–378. [CrossRef]
53. Choi, Y.; Nesic, S.; Young, D. Effect of Impurities on the Corrosion Behavior of CO_2 Transmission Pipeline Steel in Supercritical CO_2-Water Environments. *Environ. Sci. Technol.* **2010**, *44*, 9233–9238. [CrossRef] [PubMed]
54. Wang, L.; Dong, C.; Man, C.; Hu, Y.; Yu, Q.; Li, X. Effect of microstructure on Corrosion Behaviour of High Strength Martensite Steel—A literature review. *Int. J. Miner. Met. Mater.* **2021**, *28*, 754–773. [CrossRef]
55. Johnson, J.T.; Durr, C.L.; Beavers, J.A.; Delanty, B.S.; Pipelines, T. Effects of O_2 and CO_2 on Near-Neutral-pH Stress Corrosion Crack Propagation. In Proceedings of the NACE -International Corrosion Conference Series, Orlando, FL, USA, 26–31 March 2000; Volume 356, pp. 1–22.

Disclaimer/Publisher's Note: The statements, opinions and data contained in all publications are solely those of the individual author(s) and contributor(s) and not of MDPI and/or the editor(s). MDPI and/or the editor(s) disclaim responsibility for any injury to people or property resulting from any ideas, methods, instructions or products referred to in the content.